Peer-reviewed version available at Appl. Sci. 2018, 9, 17; doi:10.3390/app9010017

Article

Surface-wave extraction based on morphological diversity of seismic events

Xinming Qiu[1], Chao Wang[2,*], Jun Lu[3] and Yun Wang[4]

[1] School of Geophysics and Information Technology, China University of Geosciences (Beijing), Beijing, China

[2] The State Key Laboratory of Ore Deposit Geochemistry, Institute of Geochemistry, Chinese Academy of Sciences, Guiyang, China

[3] Key Laboratory of Marine Reservoir Evolution and Hydrocarbon Accumulation Mechanism, Ministry of Education, China University of Geosciences (Beijing), Beijing, China

* Correspondence: srmn28@163.com; Tel.: +86-156-5268-8034

Abstract: Extraction of high-resolution surface waves is essential in surface-wave survey. Because reflections usually interfere with surface waves on X component in a multicomponent seismic exploration, it is difficult to extract dispersion curves of surface waves. The situation goes more serious when the frequencies and velocities of higher-mode surface waves are close to those of PS-waves. A method for surface-wave extraction is proposed based on the morphological differences between reflections and surface waves. Frequency-domain high-resolution linear Radon transform (LRT) and time-domain high-resolution hyperbolic Radon transform (HRT) are used to represent surface waves and reflections respectively. Then, the sparse representation problem based on the morphological component analysis (MCA) is built and optimally solved to obtain high-fidelity surface waves. An advantage of our method is its ability to extract surface waves when their frequencies and velocities are close to those of reflections. Furthermore, results of synthetic and field examples confirm that the proposed method can attenuate the distortion of surface-wave dispersive energy caused by reflections, which contributes to extracting accurate dispersion curves.

Keywords: Higher-mode surface waves; dispersion curves; morphological component analysis; Radon transform

1. Introduction

Seismic surface waves are widely used in crustal and mantle structure studies and engineering prospecting, characterized by small horizontal attenuation, high signal-to-noise ratio and dispersion [1, 2]. Dispersion characteristics of surface waves reflect the near-surface S-wave velocity structure. Dispersion curves of fundamental-mode surface waves are inverted to obtain near-surface S-wave velocity structure for PS-wave static corrections in a seismic exploration [3, 4]. Recently, considering different sensitivity of fundamental- and higher-mode surface waves to elastic properties and thickness of near-surface materials, joint inversion of fundamental- and higher-mode surface waves is of wide-spread interest for less ambiguity and higher accuracy of S-wave velocities in engineering seismic prospecting, ambient seismic noise tomography and microtremor survey [5-8]. To obtain accurate S-wave velocities, extracting accurate dispersion curves of multi-mode surface waves is essential.

Fundamental-mode surface waves are dominated in vertical-component seismic data while higher-mode surface waves are generally evident on horizontal component or X component in a 2D survey [9]. Disturbed by reflections, it is usually difficult to extract accurate dispersion curves of higher-mode surface waves from X-component seismic data, causing the ambiguity of inverted S-wave velocities. Luo et al. [10] proposed high-resolution LRT to image surface-wave dispersive

energy, which improved resolution of phase velocities. But disturbed by body waves or strong noise, the dispersive energy may not be smooth and it is hard to distinguish between different modes, known as "mode kissing" [11]. This phenomenon is vulnerable to mode misidentification [12], resulting in less reliable inversion or even wrong inverted S-wave velocities.

To extract dispersion curves, surface waves are extracted on the basis of different characteristics between surface waves and interference waves. Methods of surface-wave suppression are based on single-component processing or multicomponent processing. Methods of single-component processing include f-k filtering, empirical mode decomposition and other transform methods [4, 13-15] while methods of multicomponent processing are polarization filtering and vector median filtering which preserve the vector characteristics and the spectral bandwidth of reflections [16, 17]. Pan et al. [18] discriminated the direct waves and reflections using frequency analysis. Performing a hybrid linear-hyperbolic Radon transform, Trad et al. [19] separated surface waves successfully in the signal model which consisted of both surface waves with linear events and reflections with hyperbolic events. But raw data are transformed into the conventional intercept-slowness (τ-p) domain, which is not sparse enough to separate surface waves in consideration of their dispersion characteristics. Using high-resolution LRT, Hu et al. [20] transformed raw data into the frequency-velocity (f-v) domain to implement surface-wave separation. However, it may be difficult to extract surface waves in some cases dispersive energy of higher-mode surface waves also overlaps with that of reflections in the f-v domain and then original surface-wave dispersive energy is distorted. Because the frequencies and velocities of PS-waves are close to those of higher-mode surface waves [16].

In this paper, we propose a method of surface-wave extraction to overcome the influence of reflections. The proposed method is based on the morphological differences between reflections and surface waves. We also exploit the advantages of wavefield separation by frequency-domain LRT and time-domain HRT. To implement surface-wave extraction, the sparse representation problem under the framework of MCA is optimally solved.

We firstly describe the sparse representation problem and the selected sparse dictionaries, followed by the distortion of surface-wave dispersive energy caused by reflections. Then, we demonstrate the results of surface-wave extraction and picked dispersion curves using tests with synthetic and field shot data.

2. Methods

2.1. Method of surface-wave extraction in f-v domain

High-resolution LRT is used to image surface-wave dispersive energy [10]. Using it, surface waves and reflections on Z component are clearly in different locations of f-v domain when the frequencies and velocities of them are significantly different. Hu et al. [20] extracted surface waves from Z component by a 2D window of the f-v domain.

The frequency-domain inverse LRT in the matrix-vector form is [18]:

$$\mathbf{d}(f) = \mathbf{L}(f)\mathbf{m}(f) \tag{1}$$

where $\mathbf{d}(f)$ is a vector of size $nx \times 1$ representing the Fourier coefficients of the seismic data at the given frequency f while $\mathbf{m}(f)$ is a vector of size $np \times 1$ representing the Fourier coefficients of Radon panel at the given frequency f. In equation (1), $\mathbf{L}(f)$ is a complex matrix of size $nx \times np$

Peer-reviewed version available at Appl. Sci. 2018, 9, 17; doi:10.3390/app9010017

$$\mathbf{L}(f)=\begin{bmatrix} e^{-i2\pi fx_1/v_1} & e^{-i2\pi fx_1/v_2} & \cdots & e^{-i2\pi fx_1/v_{np}} \\ e^{-i2\pi fx_2/v_1} & e^{-i2\pi fx_2/v_2} & \cdots & e^{-i2\pi fx_2/v_{np}} \\ \vdots & \vdots & \ddots & \vdots \\ e^{-i2\pi fx_{nx}/v_1} & e^{-i2\pi fx_{nx}/v_2} & \cdots & e^{-i2\pi fx_{nx}/v_{np}} \end{bmatrix} \tag{2}$$

where $v_i(\mathrm{i}=1,2,...,np)$ is the apparent velocity and $x_j(j=1,2,...,nx)$ is the offset.

The frequency-domain high-resolution forward LRT [10, 21] is inverted with a sparse constraint of a priori probability, known as:

$$\left(\lambda\mathbf{I}+\mathbf{W}_m^{-H}\mathbf{L}^H\mathbf{W}_d^H\mathbf{W}_d\mathbf{L}\mathbf{W}_m^{-1}\right)\tilde{\mathbf{m}}=\mathbf{W}_m^{-H}\mathbf{L}^H\mathbf{W}_d^H\mathbf{W}_d\mathbf{d} \tag{3}$$

where $\tilde{\mathbf{m}}=\mathbf{W}_m\mathbf{m}$. $\mathbf{W}_d$ is a matrix of data weights, a diagonal matrix showing the standard deviation, $\mathrm{diag}(\mathbf{W}_d)_i=\left|(\mathbf{d}-\mathbf{Lm})_i\right|^{-1/2}$ while $\mathbf{W}_m$ is a diagonal matrix of Radon coefficients indicating how sparse the coefficients are, $\mathrm{diag}(\mathbf{W}_m)_i=\left|m_i\right|^{-1/2}$. $\mathbf{I}$ denotes the identity matrix and the scalar λ is the tradeoff parameter that weights the relative importance of the misfit and the sparsity [22].

But it is difficult to extract surface waves correctly from X-component seismic data. Because frequencies and velocities of higher-mode surface waves and PS-waves are close and both of them are generally evident on X component. Disturbed by PS-waves, the dispersive energy is not true for surface waves. So, extracting surface waves in f-v domain is not a perfect method. We propose a method of surface-wave extraction to overcome the influence of reflections based on MCA. High-resolution LRT is one of two transforms and used to represent surface waves.

2.2. Sparse representation problem based on MCA

MCA is a method for signal separation based on sparse representations [23, 24]. It is assumed that the original signal is a linear mixture of several different parts and for each of them, there exists a dictionary which enables its construction using a sparse representation. Also, the dictionary can only sparsely represent the corresponding part rather than others. For seismic data consisting of surface waves and reflections, there is

$$\mathbf{y}=\mathbf{y}_{\mathrm{g}}+\mathbf{y}_{\mathrm{r}} \tag{4}$$

where $\mathbf{y}$ is the seismic data set, $\mathbf{y}_{\mathrm{g}}$ is the surface-wave part and $\mathbf{y}_{\mathrm{r}}$ is the reflection part. We choose $\mathbf{D}_{\mathrm{g}}$ and $\mathbf{D}_{\mathrm{r}}$ as the sparse representation dictionaries of surface waves and reflections respectively, i.e., $\mathbf{y}_{\mathrm{g}}=\mathbf{D}_{\mathrm{g}}\mathbf{z}_{\mathrm{g}}$, $\mathbf{y}_{\mathrm{r}}=\mathbf{D}_{\mathrm{r}}\mathbf{z}_{\mathrm{r}}$. Separation of surface waves and reflections can be formulated as [25]:

$$\underset{\{\mathbf{z}_{\mathrm{g}},\mathbf{z}_{\mathrm{r}}\}}{\operatorname{argmin}}\frac{1}{2}\left\|\mathbf{y}-\mathbf{D}_{\mathrm{g}}\mathbf{z}_{\mathrm{g}}-\mathbf{D}_{\mathrm{r}}\mathbf{z}_{\mathrm{r}}\right\|_2^2+\mu(\left\|\mathbf{z}_{\mathrm{g}}\right\|_1+\left\|\mathbf{z}_{\mathrm{r}}\right\|_1) \tag{5}$$

where $\mathbf{z}_{\mathrm{g}}$ and $\mathbf{z}_{\mathrm{r}}$ are the representation vectors for surface waves and reflections, respectively, and μ is the regularization parameter.

Surface waves are generally modeled as broom-like events characterized by low frequency, low velocity and dispersion, and their dispersive energy is around theoretical dispersion curves in the f-v domain [20, 26]. Therefore, frequency-domain high-resolution LRT can sparsely represent surface waves in theory. Reflections are approximated by hyperbolas and time-domain high-resolution HRT

can sparsely represent reflections with assumptions that velocities change little horizontally and reflection interfaces are almost horizontal [27]. We choose frequency-domain high-resolution LRT and time-domain high-resolution HRT to represent surface waves and reflections respectively. To match with the matrix definition of sparse representation dictionaries in our sparse representation problem, the inverse LRT and inverse HRT correspond to the matrix signs $\mathbf{D}_{\mathrm{g}}$ and $\mathbf{D}_{\mathrm{r}}$ respectively while the forward LRT and forward HRT are respectively the matrices $\mathbf{D}_{\mathrm{g}}^{+}$ and $\mathbf{D}_{\mathrm{r}}^{+}$. The matrices $\mathbf{D}_{\mathrm{g}}^{+}$ and $\mathbf{D}_{\mathrm{r}}^{+}$ are pseudo inverse of the representation dictionaries, i.e., $\mathbf{z}_{\mathrm{g}}=\mathbf{D}_{\mathrm{g}}^{+}\mathbf{y}_{\mathrm{g}}$, $\mathbf{z}_{\mathrm{r}}=\mathbf{D}_{\mathrm{r}}^{+}\mathbf{y}_{\mathrm{r}}$. Put these back into (5) we obtain

$$\underset{\{\mathbf{y}_{\mathrm{g}},\mathbf{y}_{\mathrm{r}}\}}{\operatorname{argmin}}\frac{1}{2}\left\|\mathbf{y}-\mathbf{y}_{\mathrm{g}}-\mathbf{y}_{\mathrm{r}}\right\|_{2}^{2}+\mu\left(\left\|\mathbf{D}_{\mathrm{g}}^{+}\boldsymbol{y}_{\mathrm{g}}\right\|_{1}+\left\|\mathbf{D}_{\mathrm{r}}^{+}\mathbf{y}_{\mathrm{r}}\right\|_{1}\right) \tag{6}$$

which is solved by generalized BCR algorithm [23].

Surface waves is extracted by solving equation (6). Different dictionaries are respectively chosen to represent surface waves and reflections so that the influence of reflections on surface-wave dispersive energy is reduced.

2.2.1. Frequency-domain high-resolution LRT

To sparsely represent surface waves, equation (3) is solved to achieve high-resolution LRT in the spectral bandwidth of surface waves by iteratively reweighted least squares (IRLS) algorithm [28]. The choice of the apparent-velocity range and interval should avoid aliasing [29] for reconstruction; moreover, the apparent-velocity range includes the phase velocities of surface waves.

2.2.2. Time-domain high-resolution HRT

Inverse and adjoint HRT in the discrete form can be expressed as [30]:

$$d(t,x)=\sum_{v}m\left(\tau=\sqrt{t^{2}-x^{2}/v^{2}},v\right) \tag{7}$$

and

$$m_{\mathrm{adj}}(\tau,v)=\sum_{x}d\left(t=\sqrt{\tau^{2}+x^{2}/v^{2}},x\right) \tag{8}$$

where $d(t,x)$ are the seismic data in time-offset domain, x indicates the offset, t donates two-way time, $m(\tau,v)$ are the Radon coefficients, v indicates the root-mean-square velocity of a reflection, τ donates the time intercept, $m_{\mathrm{adj}}(\tau,v)$ are the low resolution Radon coefficients. Equations (7) and (8) are represented in matrix-vector form as follows [30]:

$$\mathbf{d}=\mathbf{L}\mathbf{m} \tag{9}$$

$$\mathbf{m}_{\mathrm{adj}}=\mathbf{L}^{T}\mathbf{d} \tag{10}$$

where $\mathbf{d}$ is a vector of size $N\times 1$ whose elements are taken trace-wise from the seismic data ($N=nx\times nt$) and $\mathbf{m}$ is a vector of size $M\times 1$ whose elements are taken velocity-wise from the Radon coefficients ($M=nv\times n\tau$). nx, nt, nv and $n\tau$ are the number of traces, samples, velocities and time intercepts respectively. In equation (9) and (10), the operators $\mathbf{L}$ and $\mathbf{L}^{T}$ are just represented for the summation algorithms shown in equation (7) and (8) instead of matrices [31].

High-resolution forward HRT can be inverted from equation (9) using a sparse constraint satisfying

$$(\mathbf{W}_{m}^{T}\mathbf{W}_{m})^{-1}\mathbf{L}^{T}\mathbf{W}_{d}^{T}\mathbf{W}_{d}\mathbf{L}\mathbf{m}=(\mathbf{W}_{m}^{T}\mathbf{W}_{m})^{-1}\mathbf{L}^{T}\mathbf{W}_{d}^{T}\mathbf{W}_{d}\mathbf{d} \tag{11}$$

which is solved by a left preconditioned version of conjugate gradient for the normal equations algorithm [31].

The computational cost of applying operators $\mathbf{L}$ and $\mathbf{L}^T$ is controlled by the size of the Radon domain [32]. To speed up the implementation, time-domain high-resolution forward HRT is solved in the restricted Radon space [32]

$$(\mathbf{W}_{m_{\mathbb{A}}}^T \mathbf{W}_{m_{\mathbb{A}}})^{-1} \mathbf{L}_{\mathbb{A}}^T \mathbf{W}_d^T \mathbf{W}_d \mathbf{L}_{\mathbb{A}} \mathbf{m}_{\mathbb{A}} = (\mathbf{W}_{m_{\mathbb{A}}}^T \mathbf{W}_{m_{\mathbb{A}}})^{-1} \mathbf{L}_{\mathbb{A}}^T \mathbf{W}_d^T \mathbf{W}_d \mathbf{d} \tag{12}$$

where $\mathbf{d}$ should be normalized to unity by dividing the maximum of the seismic data [33]. The restricted Radon space is defined as

$$\mathbb{A} = \left\{ (\tau, p) : \frac{1}{nx} \left| \mathbf{m}_{\text{adj}} \right| > T \right\} \tag{13}$$

where T is the threshold satisfying $0 < T < 1$.

2.2.3. Performance of sparse representations using LRT and HRT

We synthesized the surface waves (Figure 1) of the two-horizontal-layer model (Model 1) described by Table 1 using a staggered-grid finite-difference method. Then we synthesized reflections (Figure 2) of the three-horizontal-layer model (Model 2) described by Table 2 using ray tracing. Frequency-domain high-resolution forward LRT and time-domain high-resolution forward HRT are applied to the surface waves and reflections to get the four panels of the Radon coefficients. Next, we respectively normalized the Radon coefficients to unity divided by the maximum of each panel and apply hard threshold to them. Finally, the seismic data were reconstructed by the inverse transforms. For a Radon panel, the higher threshold amplitude means the fewer Radon coefficients used in the reconstruction.

To confirm the effectiveness of sparse representations for surface waves and reflections, the reconstruction error is calculated as follows:

$$err = \sum_x E_x^r \Big/ \sum_x E_x^0 \tag{14}$$

where E_x^r represents the root-mean-square error between reconstruction and original data at the offset x, i.e., $E_x^r = \sqrt{\frac{1}{nt} \sum_t \left(d(t,x) - \tilde{d}(t,x) \right)^2}$, $\tilde{d}(t,x)$ represent the reconstruction data, and $E_x^0 = \sqrt{\frac{1}{nt} \sum_t \left(d(t,x) \right)^2}$ represents the root-mean-square value of original data at the offset x, i.e., $E_x^0 = \sqrt{\frac{1}{nt} \sum_t \left(d(t,x) \right)^2}$. The reconstruction errors against the threshold amplitude are illustrated in Figure 3. According to Figure 3a, fewer coefficients can be used to similarly reconstruct the surface waves by frequency-domain high-resolution LRT compared with time-domain high-resolution HRT, which means the former can represent surface waves more sparsely. On the basis of Figure 3b, time-domain high-resolution HRT can represent reflections more sparsely than frequency-domain high-resolution LRT. Comparing the HRT-reconstruction errors shown by dashed lines between Figure 3a and Figure 3b, time-domain high-resolution HRT leads to a non-sparse representation for surface waves. Similarly, frequency-domain high-resolution LRT leads to a non-sparse representation for reflections comparing the LRT-reconstruction errors. Thus, the two transforms (dictionaries) are significantly different in the sparse representations for surface waves and reflections, which meets the assumptions of MCA, and it is theoretically feasible to extract the surface waves based on equation (6).

Peer-reviewed version available at Appl. Sci. 2018, 9, 17; doi:10.3390/app9010017

183 **Table 1.** Parameters of Model 1.

Thickness (m)	Vp (m/s)	Vs (m/s)	Density (kg/m³)
10	800	200	2000
-	1200	400	2000

184 **Table 2.** Parameters of Model 2.

Thickness (m)	Vp (m/s)	Vs (m/s)	Density (kg/m³)
100	1200	400	2000
150	2200	1320	2250
-	3300	2045	2400

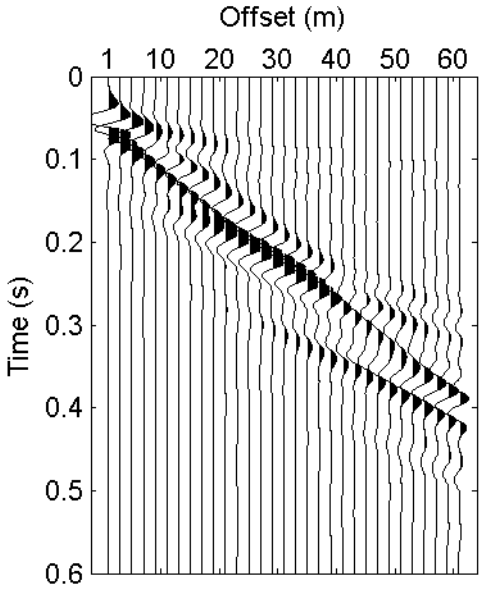

185

186 **Figure 1.** Synthetic seismic data (mainly surface waves) of Model 1.

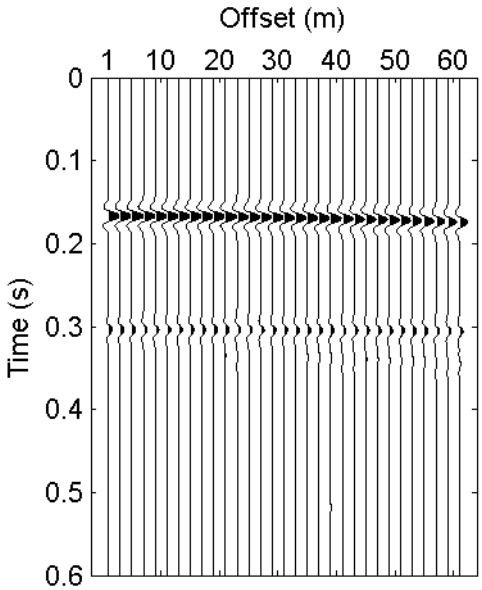

187

188 **Figure 2.** Synthetic reflections of Model 2.

Preprints (www.preprints.org) | NOT PEER-REVIEWED | Posted: 17 October 2018 doi:10.20944/preprints201810.0356.v2

Peer-reviewed version available at Appl. Sci. 2018, 9, 17; doi:10.3390/app9010017

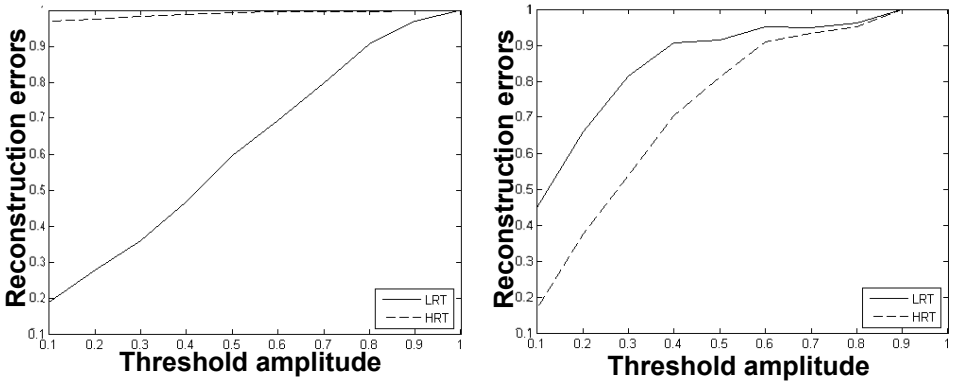

Figure 3. Curves of the reconstruction errors of (a) surface waves and (b) reflections against the threshold amplitude.

3. Examples

3.1. Synthetic examples

3.1.1. Distortion of surface-wave dispersive energy caused by reflections

Two layered earth models (Model 3 and Model 4) are given in Table 3 and 4 to display the distortion of surface-wave dispersive energy caused by reflections. The layers of Model 3 are the first two layers of Model 4. A synthetic X-component shot gather (Figure 4a) of the Model 3 is simulated using a staggered-grid finite-difference method with an explosive source located at 3-m depth. Another synthetic X-component shot gather (Figure 5a) of the Model 4 is simulated using the same method and the same forward-simulation parameters. We simulated the records with 51 receivers evenly spaced 2 m in line on the surface and the nearest offset of 40 m. As shown in Figure 4b and 5b, the two shot gathers are transformed into the f-v domain by high-resolution LRT.

According to the relationship between penetration depths of Rayleigh waves and wavelengths [34], the surface waves of Model 3 and Model 4 can't penetrate into the depth of 100 m so the dispersion characteristics of pure surface waves in Figure 5a should be similar to that in Figure 4a. The surface waves in Figure 4a are not disturbed by the reflections from the deep reflectors. The dispersive energy shown in Figure 4b is continuous and the three branches of dispersion energy are clearly corresponding to the first, second, third higher modes. But the events of higher-mode surface waves in Figure 5a are discontinuous overlapping with the reflections in two-way time of 0.35 s and 0.45 s, and it is difficult to discern which higher mode the dispersive energy in frequencies of 25-33 Hz and apparent velocities of 470-530 m/s (energy circled in Figure 5b) corresponds to. A comparison of Figure 4b and Figure 5b demonstrates that reflections may disturb the dispersive energy of surface waves. What causes this phenomenon "mode kissing" is the non-negligible effect of the reflections at the range of frequencies and velocities. The picked dispersion curves based on the amplitude and the continuity of dispersive energy are shown in Figure 5c where the second higher mode of frequencies of 25-27 Hz mistakes for the third higher mode. However, the surface-wave dispersive energy on Z-component seismic data is not severely influenced by the reflections from the deep reflectors according to Hu et al. [20].

Table 3. Parameters of Model 3.

Thickness (m)	Vp (m/s)	Vs (m/s)	Density (kg/m³)
10	800	200	2000
90	1200	600	2000

222 **Table 4.** Parameters of Model 4.

Thickness (m)	Vp (m/s)	Vs (m/s)	Density (kg/m³)
10	800	200	2000
90	1200	600	2000
600	2200	1320	2250
-	3300	2045	2400

223

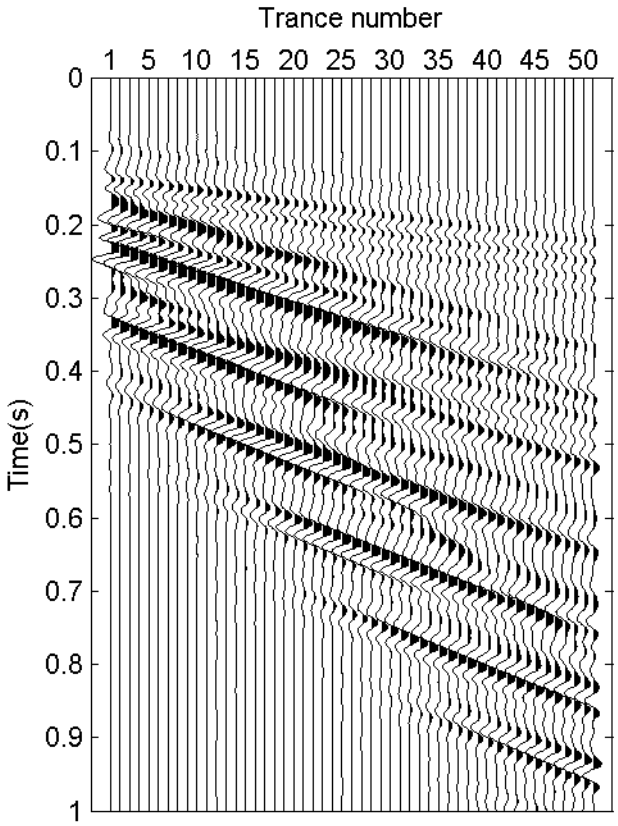

(a)

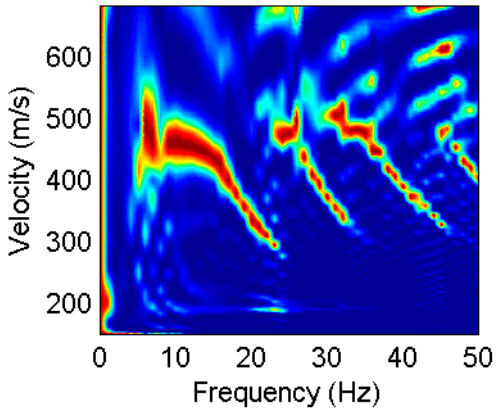

(b)

224 **Figure 4.** (a) A synthetic X-component shot gather of Model 3 and (b) its image of dispersive energy
225 in the f-v domain where the white dotted lines represent the theoretical dispersion curves.

Preprints (www.preprints.org) | NOT PEER-REVIEWED | Posted: 17 October 2018 doi:10.20944/preprints201810.0356.v2

Peer-reviewed version available at Appl. Sci. 2018, 9, 17; doi:10.3390/app9010017

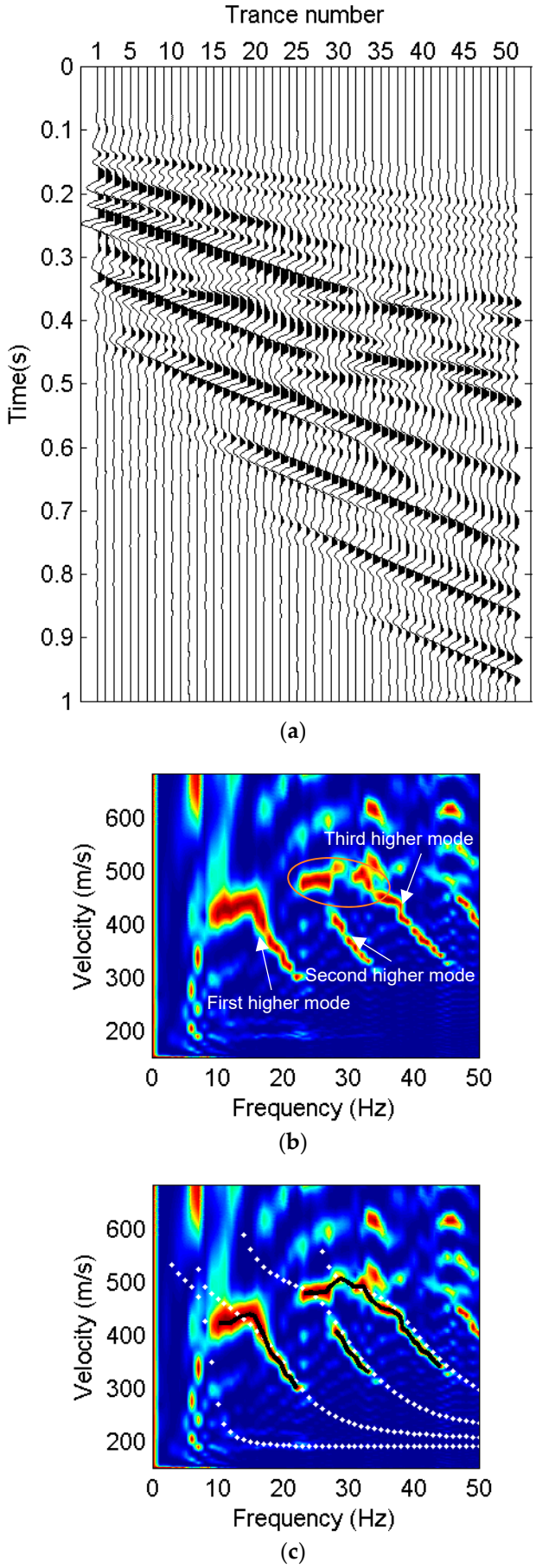

Figure 5. (a) A synthetic X-component shot gather of Model 4, (b) its image of dispersive energy in the f-v domain and (c) dispersion curves picked from the dispersive energy.

Peer-reviewed version available at Appl. Sci. 2018, 9, 17; doi:10.3390/app9010017

3.1.2. Recovery of the surface-wave dispersive energy

The proposed method is applied to the synthetic seismic data shown in Figure 5a to display the result of surface-wave extraction and the improvement of the surface-wave dispersive energy. Compared with the dispersive energy of the original seismic data shown in Figure 5b, the dispersive energy of the surface waves extracted from the data is more continuous in Figure 6. The energy of 25-27 Hz and 28-33 Hz is separated to two parts corresponding to the second higher mode and the third higher mode respectively, which means "mode kissing" disappears. Also, the dispersive energy is close to the theoretical dispersion curves, which implies surface waves are effectively extracted using the proposed method.

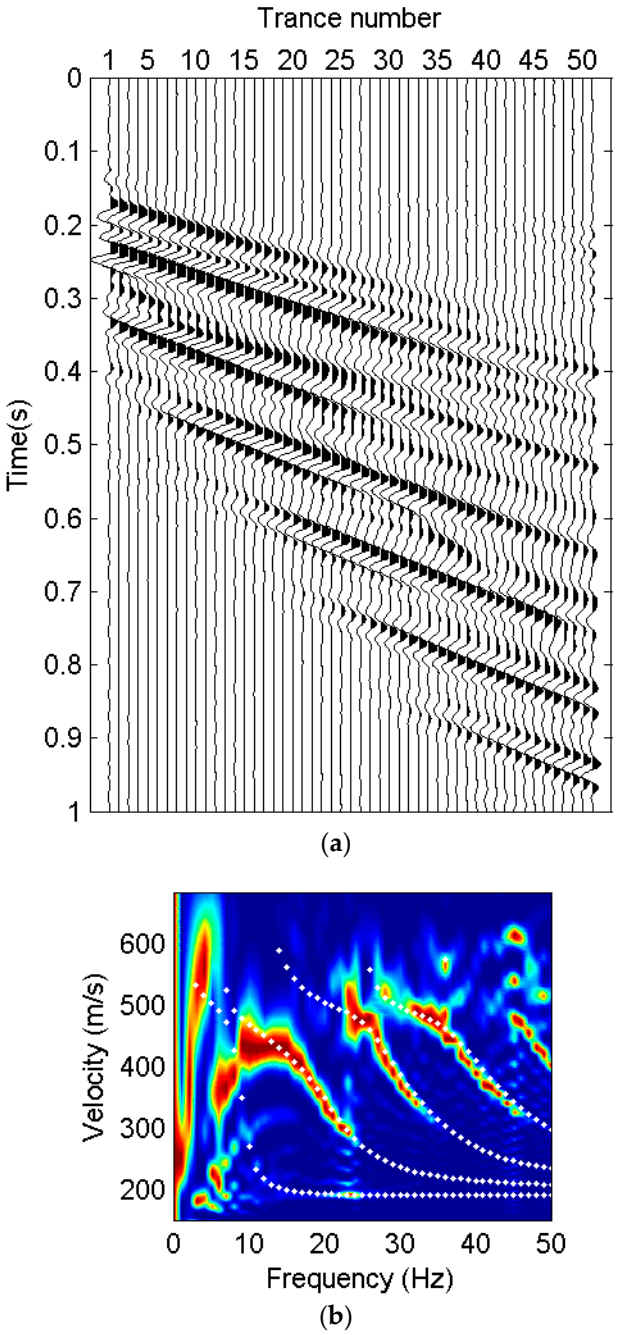

Figure 6. (a) Result of surface-wave extraction by the proposed method and (b) its image of dispersive energy in the f-v domain where the white dotted lines represent the theoretical dispersion curves.

Furthermore, we compared the proposed method with other methods of surface-wave extraction to test the superiority of the proposed method. High-resolution LRT is applied to the original data and a 2D window is used to select and extract surface waves in the f-v domain. In Figure

7, the result shows surface waves are mainly extracted but "mode kissing" is not changed. The f-k filtering method is also used to extract surface waves. The result of surface-wave extraction consists of residual reflections in Figure 8a and "mode kissing" is reduced in Figure 8b. But there is also a risk of mode misidentification owing to the discontinuous dispersive energy shown in Figure 8b.

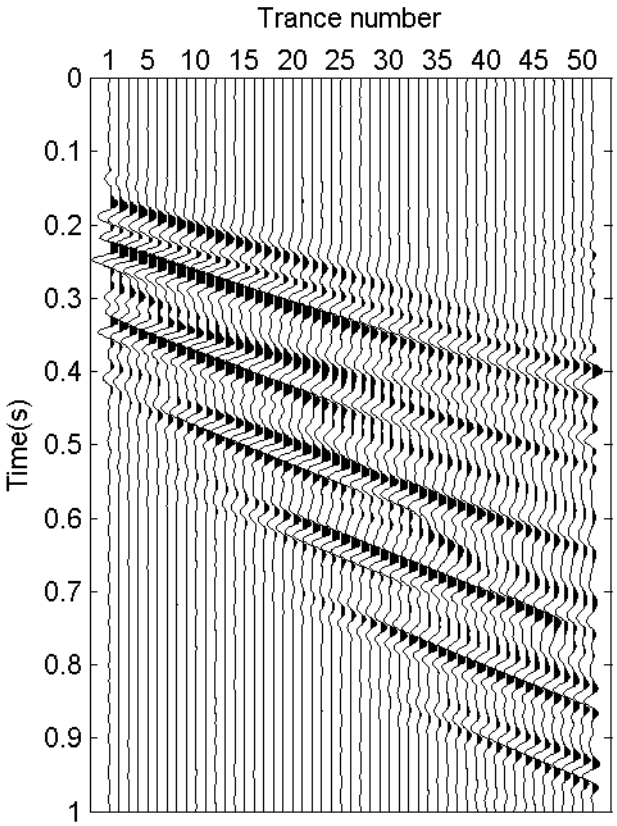

(a)

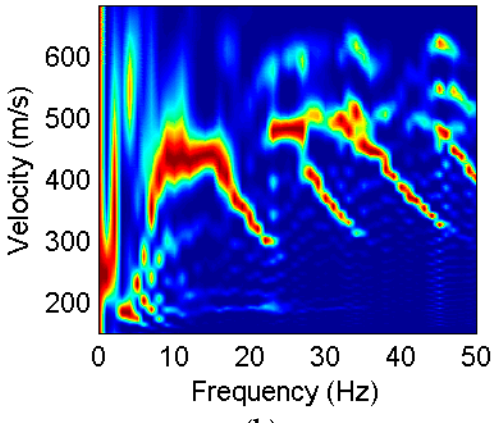

(b)

Figure 7. (a) Result of surface-wave separation by a 2D window of the f-v domain and (b) its image of dispersive energy in the f-v domain.

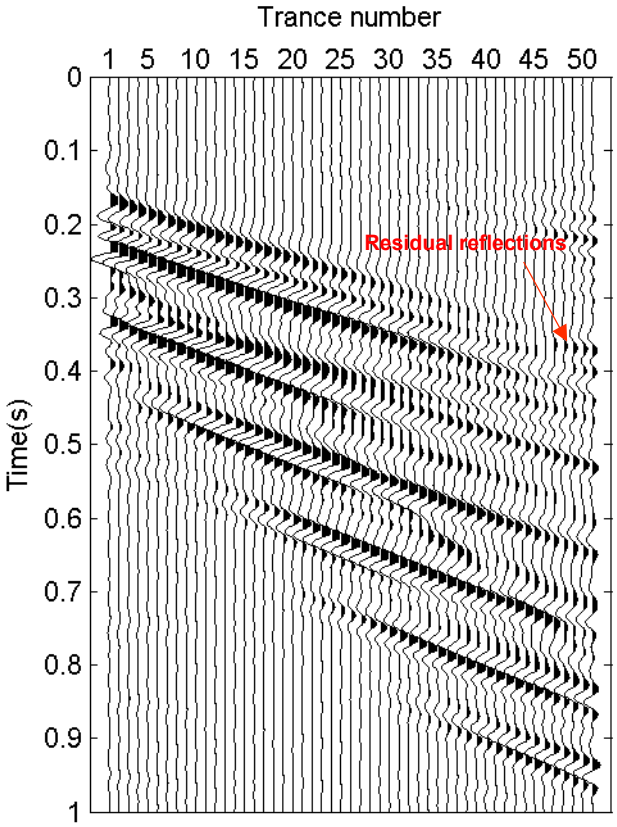

(**a**)

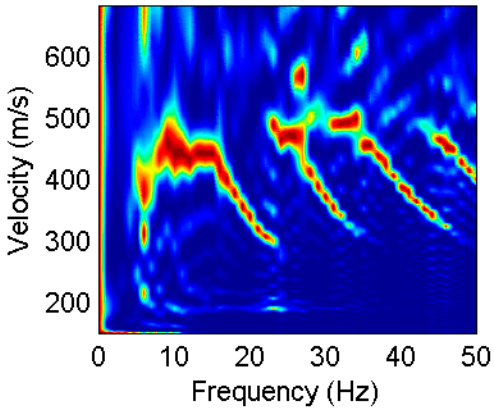

(**b**)

Figure 8. (a) Result of surface-wave separation by f-k filtering and (b) its image of dispersive energy in the f-v domain.

3.2. A field example

The X-component field data of 2D3C seismic data shown in Figure 9 were acquired in the Wangjiatun District, Daqing Oilfield, China, with the sample interval of 4 ms, the geophone interval of 25 m and the nearest offset of 400 m. It can be seen that several events of higher-mode surface waves overlap with the reflections. Reflections spread over the f-v domain while surface waves are mainly at the range of low frequencies and low velocities shown in Figure 10. Several branches of dispersive energy at frequencies of ~5 Hz and velocities of 800-1000 m/s circled in Figure 10 are so close to each other resulting in inaccurate phase velocities at those frequencies. By the proposed method, the extracted surface waves are shown in Figure 11a, where most of surface waves are extracted, and the rest of the field data are reflections and other noise except for small amount of

surface waves circled in Figure 11b. This is because the morphology of surface waves and reflections may not meet the assumption occasionally in view of the near surface heterogeneity.

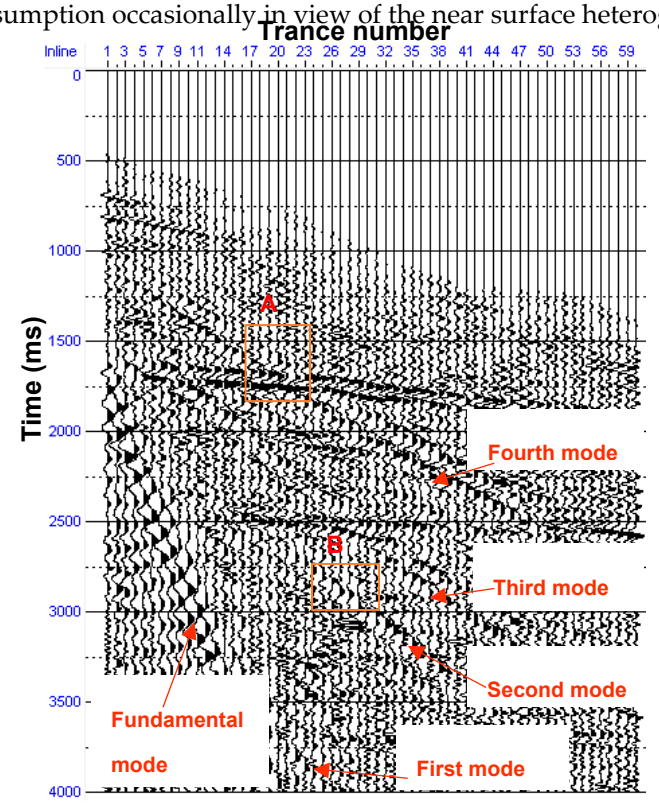

Figure 9. X-component field data of 2D3C seismic data acquired in the Wangjiatun District, Daqing Oilfield, China.

Preprints (www.preprints.org) | NOT PEER-REVIEWED | Posted: 17 October 2018 doi:10.20944/preprints201810.0356.v2

Peer-reviewed version available at Appl. Sci. 2018, 9, 17; doi:10.3390/app9010017

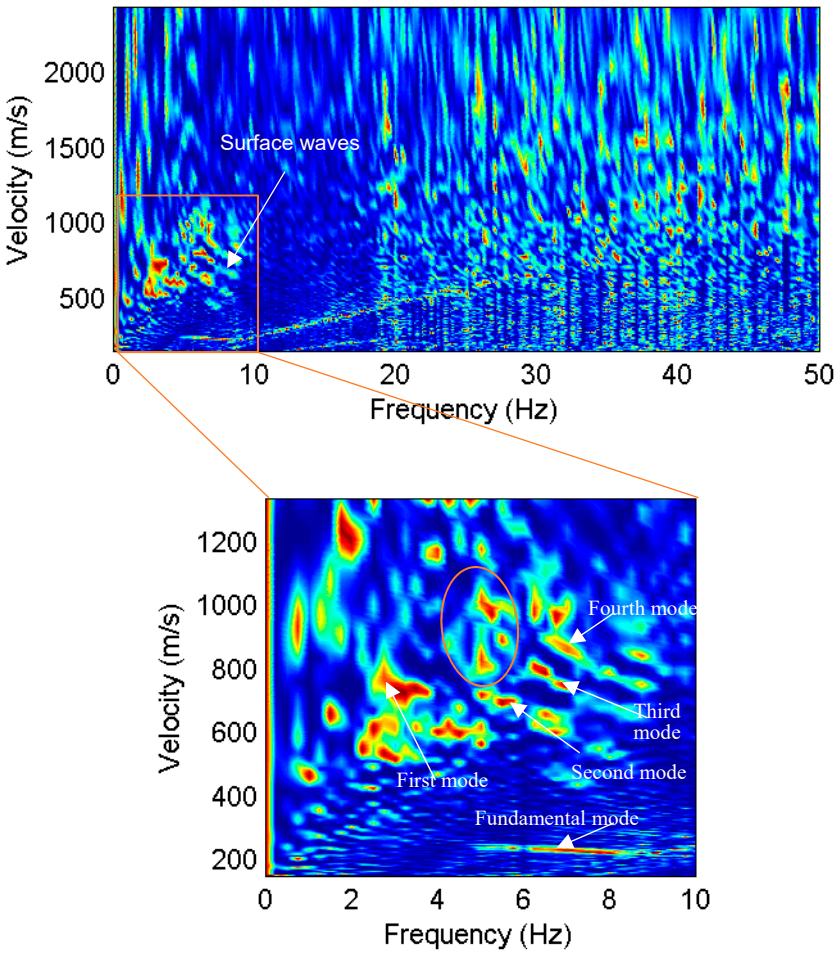

Figure 10. Image of dispersive energy of the field data in the f-v domain

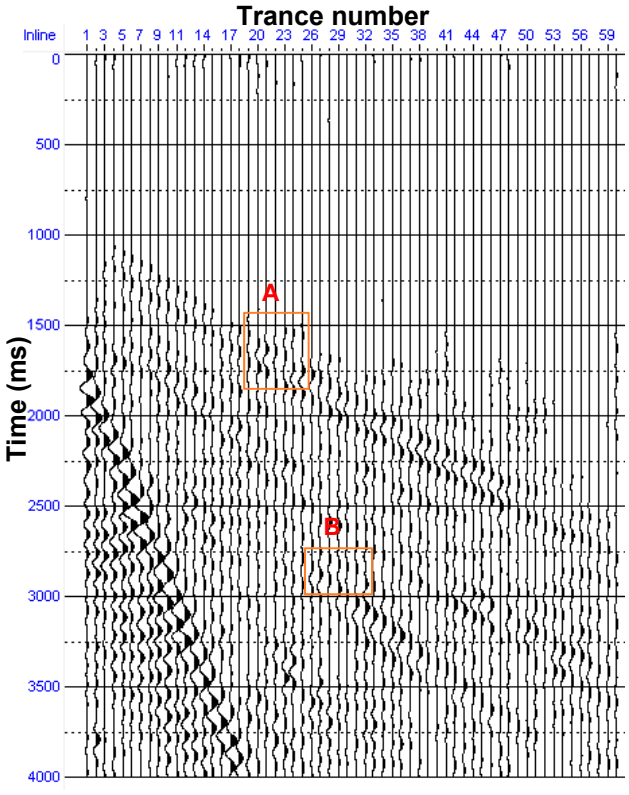

(**a**)

Preprints (www.preprints.org) | NOT PEER-REVIEWED | Posted: 17 October 2018 doi:10.20944/preprints201810.0356.v2

Peer-reviewed version available at Appl. Sci. 2018, 9, 17; doi:10.3390/app9010017

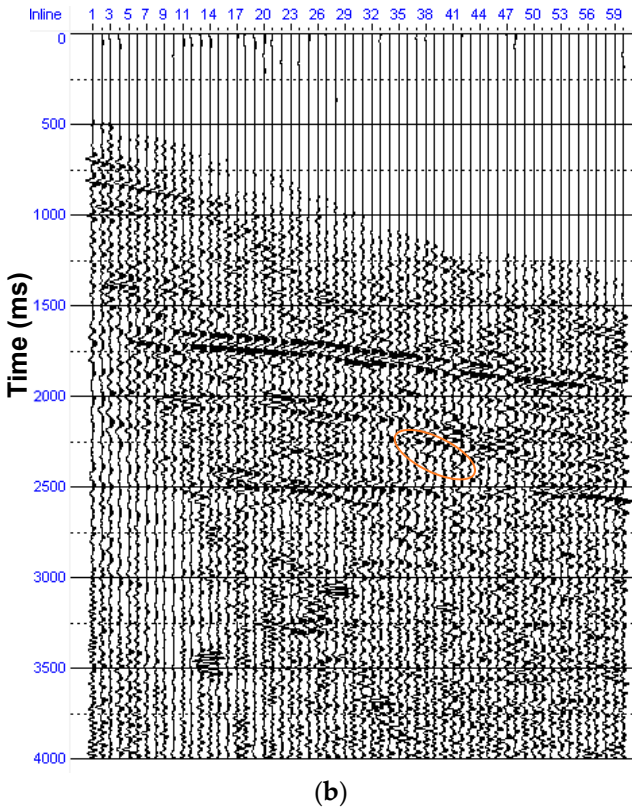

Figure 11. (a) Extracted surface waves by the proposed method and (b) the rest of the field data.

To display the effectiveness of surface-wave extraction further, the details of waveform are compared in Figure 12 where the original field data (Figure 9) and the result of surface-wave extraction (Figure 11a) in section A and section B are zoomed. For section A, the original data are dominated by reflections while the surface waves can be easily identified in the result of surface-wave extraction. For section B, surface waves are more clearly and more continuous after surface-wave extraction. The image of dispersive energy of the extracted surface waves using the proposed method is shown in Figure 13a. After surface-wave extraction, the dispersive energy of different modes is separated and the ambiguity of the phase velocities in Figure 10 is eliminated. As shown in Figure 13b, we can easily pick dispersion curves from Figure 13a. For comparison, the dispersive energy of surface waves separated by the f-k filtering method is displayed in Figure 14, where it is difficult to identify the modes of circled energy. The results of the synthetic example and the field example demonstrate that surface-wave extraction by the proposed method attenuates the distortion of the surface-wave dispersive energy caused by reflections, which contributes to extracting accurate dispersion curves.

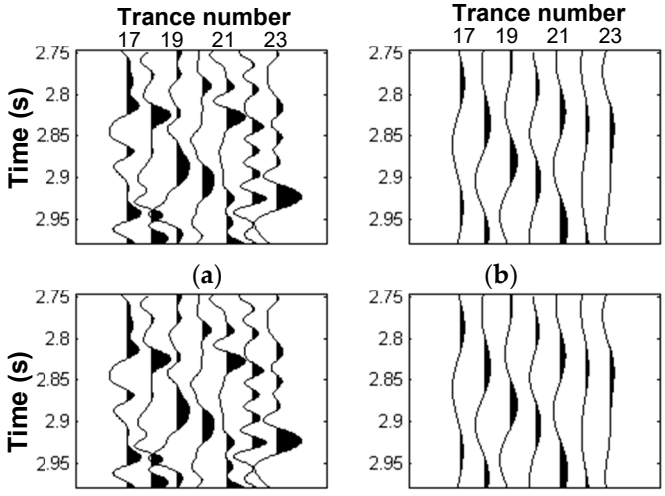

(c) (d)

Figure 12. Details of waveform of (a) section A in Figure 9, (b) section A in Figure 11a, (c) section B in Figure 9 and (d) section B and Figure 11a.

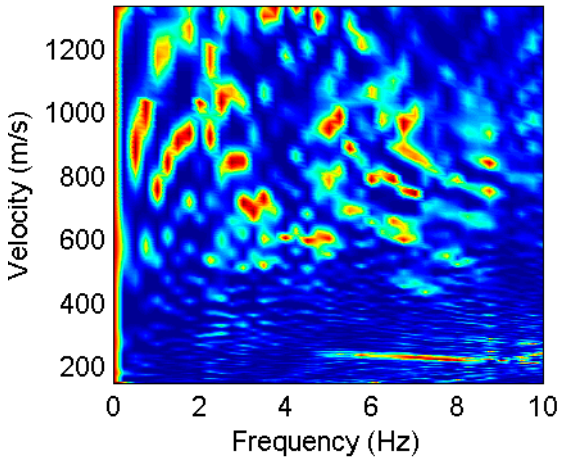

(a)

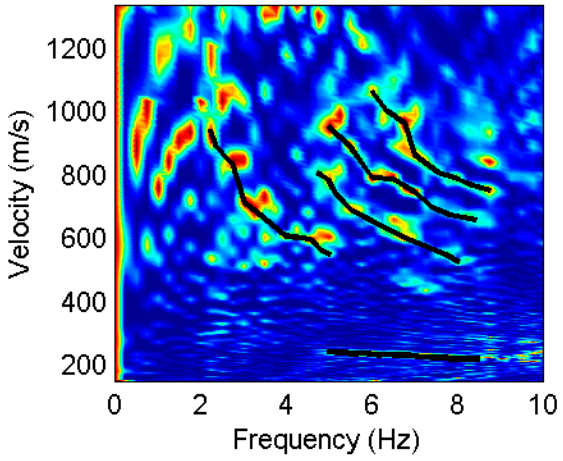

(b)

Figure 13. (a)Image of dispersive energy of the extracted surface waves using the proposed method and (b) dispersion curves picked from Figure 13a.

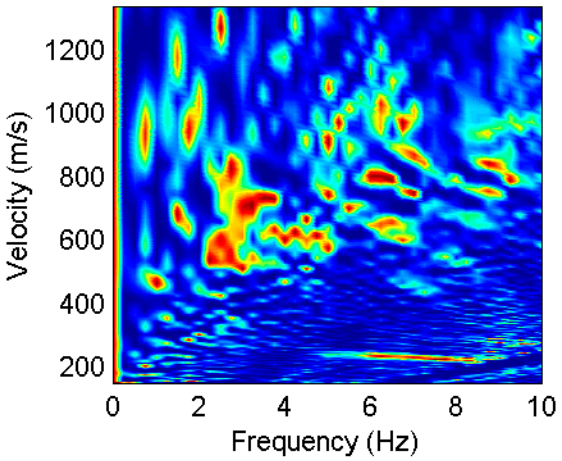

Figure 14. Image of dispersive energy of the extracted surface waves by f-k filter.

4. Discussion

The advantage of the method over other methods of surface-wave extraction is clear for X-component seismic data while it is not obvious for Z component. The surface-wave dispersive energy on Z component is not severely influenced by the reflections because surface waves and reflections on Z component are clearly in different locations of f-v domain for Z-component seismic data (Hu et al., 2016) where fundamental-mode surface waves are dominated.

The main limitation of the method is that surface waves and reflections may not be separated thoroughly in field data. The main problem is that the morphology of surface waves and reflections may deviate the assumption in view of the near surface heterogeneity. In addition, the reflections are not represented by high-resolution HRT sparsely for steep-reflection interfaces so that the surface-wave dispersive energy can't avoid the influence of reflections. Further research will be conducted to solve the problems.

5. Conclusion

We propose a method to extract surface waves by exploiting the morphological differences between reflections and surface waves on the basis of MCA. The advantage of this method over the previous techniques is that it can extract surface waves in the case where dispersive energy of higher-mode surface waves overlaps with that of reflections in the f-v domain. It may allow one to separate PS-waves and surface waves whose frequencies and velocities are close. Synthetic and field examples demonstrate that: (1) Frequency-domain high-resolution LRT and time-domain high-resolution HRT are significantly different in the sparse representations for surface waves and reflections, which is suitable for wavefield separation; (2) Reflections may disturb the dispersive energy of surface waves, which makes it difficult to extract dispersion curves of surface waves; (3) Surface waves are effectively extracted by the proposed method and the dispersive energy becomes more continuous and less distorted. Also, dispersion curves picked from the dispersive energy are much more accurate in view of the reliable image of surface-wave dispersive energy.

Funding: This research is financially supported by the National Natural Science Foundation of China (Grant Nos. 41425017,41504107,41874166).

Acknowledgments: The first author appreciates Jianjun Gao and Chunying Yang for their constructive suggestions on Radon transform and its application to dispersion curve extraction.

References

1. Xia, J.H.; Miller, R.D.; Park, C.B.; Ivanov, J.; Tian, G.; Chen, C. Utilization of High-Frequency Rayleigh Waves in near-Surface Geophysics. *Leading Edge* **2004**, 23, 753-759, doi:10.1190/1.1786895.
2. Zhang, Z.; Chen, Y.; Li, F. Reconstruction of the S-Wave Velocity Structure of Crust and Mantle from Seismic Surface Wave Dispersion in Sichuan-Yunnan Region. *Chinese Journal of Geophysics (in Chinese)* **2008**, 51, 1114-1122, doi:10.3321/j.issn:0001-5733.2008.04.020.
3. Yang, C.Y.; Wang, Y.; Lu, J. Application of Rayleigh Waves on Ps-Wave Static Corrections. *Journal of Geophysics & Engineering* **2012**, 9, 90-97, doi:10.1088/1742-2132/9/1/011.
4. Meng, X.H.; Guo, L.H. Using Velocity Inversion of Seismic Rayleigh Wave to Compute S-Wave Statics of P-Sv Wave. *Oil Geophysical Prospecting (in Chinese)* **2007**, 42, 448-453, doi:10.3321/j.issn:1000-7210.2007.04.017.
5. Luo, Y.H.; Xia, J.H.; Liu, J.P. Joint Inversion of Fundamental and Higher Mode Rayleigh Waves. *Chinese Journal of Geophysics (in Chinese)* **2008**, 51, 242-249, doi:10.3321/j.issn:0001-5733.2008.01.030.
6. Xia, J.H.; Miller, R.D.; Park, C.B.; Tian, G. Inversion of High Frequency Surface Waves with Fundamental and Higher Modes. *Journal of Applied Geophysics* **2003**, 52, 45-57, doi:10.1016/s0926-9851(02)00239-2.
7. Zhou, X.H.; Lin, J.; Zhang, H.Z.; Jiao, J. Mapping Extraction Dispersion Curves of Multi-Mode

Rayleigh Waves in Microtremors. *Chinese Journal of Geophysics (in Chinese)* **2014**, 57, 2631-2643, doi:10.6038/cjg20140822.

8. Kimman, W.P.; Campman, X.; Trampert, J. Characteristics of Seismic Noise: Fundamental and Higher Mode Energy Observed in the Northeast of the Netherlands. *Bulletin of the Seismological Society of America* **2012**, 102, 1388-1399, doi:10.1785/0120110069.
9. Savage, M.K.; Lin, F.C.; Townend, J. Ambient Noise Cross-Correlation Observations of Fundamental and Higher-Mode Rayleigh Wave Propagation Governed by Basement Resonance. *Geophysical Research Letters* **2013**, 40, 3556-3561, doi:10.1002/grl.50678.
10. Luo, Y.H.; Xia, J.H.; Miller, R.D.; Xu, Y.X.; Liu, J.P.; Liu, Q.S. Rayleigh-Wave Dispersive Energy Imaging Using a High-Resolution Linear Radon Transform. *Pure and Applied Geophysics* **2008**, 165, 903-922, doi:10.1007/s00024-008-0338-4.
11. Xia, J.H.; Xu, Y.X.; Luo, Y.H.; Miller, R.D.; Cakir, R.; Zeng, C. Advantages of Using Multichannel Analysis of Love Waves (Malw) to Estimate near-Surface Shear-Wave Velocity. *Surveys in Geophysics* **2012**, 33, 841-860, doi:10.1007/s10712-012-9174-2.
12. Zhang, S.X.; Chan, L.S. Possible Effects of Misidentified Mode Number on Rayleigh Wave Inversion. *Journal of Applied Geophysics* **2003**, 53, 17-29, doi:10.1016/s0926-9851(03)00014-4.
13. Bao, Q.Z.; Gao, J.H.; Chen, W.C. Ridgelet Domain Method of Ground-Roll Suppression. *Chinese Journal of Geophysics* **2007**, 50, 1041-1047.
14. Fang, Y.R.; Shen, F.M.; Qiu, K.N. The New Method of Rayleigh Wave Signal Purification Based on Emd. *Earthquake Engineering & Engineering Dynamics* **2017**, 01, 64-71.
15. Li, J.F.; Li, R.H.; Wang, W.D. Study on the Extraction of Effective Wave Using Analytic Signal Method in Multicomponent Rayleigh Wave Exploration. *Coal Geology & Exploration* **1998**, 26, 61-64.
16. Lu, J.; Yun, W.; Yang, C.Y. Instantaneous Polarization Filtering Focused on Suppression of Surface Waves. *Applied Geophysics* **2010**, 7, 88-97, doi:10.1007/s11770-010-0001-6.
17. Lu, J.; Wang, Y.; Chen, J.Y. Noise Attenuation Based on Wave Vector Characteristics. *Applied Sciences* **2018**, 8, 672, doi:10.3390/app8050672.
18. Pan, D.; Hu, M.; Cui, R.; Li, J. Dispersion Analysis of Rayleigh Surface Waves and Application Based on Radon Transform. *Chinese Journal of Geophysics (in Chinese)* **2010**, 53, 2760-2766, doi:10.3969/j.issn:0001-5733.2010.11.025.
19. Trad, D.; Sacchi, M.D.; Ulrych, T.J. A Hybrid Linear-Hyperbolic Radon Transform. *Journal of Seismic Exploration* **2001**, 9, 303-318.
20. Hu, Y.; Wang, L.M.; Cheng, F.; Luo, Y.H.; Shen, C.; Mi, B.B. Ground-Roll Noise Extraction and Suppression Using High-Resolution Linear Radon Transform. *Journal of Applied Geophysics* **2016**, 128, 8-17, doi:10.1016/j.jappgeo.2016.03.007.
21. Sacchi, M.D.; Ulrych, T.J. High-Resolution Velocity Gather and Offset Space Reconstruction. *Geophysics* **1995**, 60, 1169-1177, doi:10.1190/1.1443845.
22. Trad, D.; Ulrych, T.J.; Sacchi, M.D. Latest Views of the Sparse Radon Transform. *Geophysics* **2003**, 68, 386--399, doi:10.1190/1.1543224.
23. Starck, J.L.; Elad, M.; Donoho, D.L. Redundant Multiscale Transforms and Their Application for Morphological Component Separation. *Advances in Imaging & Electron Physics* **2004**, 132, 287-348, doi:10.1016/s1076-5670(04)32006-9.
24. Starck, J.L.; Elad, M.; Donoho, D.L. Image Decomposition Via the Combination of Sparse Representations and a Variational Approach. *IEEE Transactions on Image Processing* **2005**, 14, 1570-

1582, doi:10.1109/tip.2005.852206.

25. Chen, W.C.; Wang, W.; Gao, J.H.; Jiang, C.F.; Lei, J.L. Sparsity Optimized Separation of Ground-Roll Noise Based on Morphological Diversity of Seismic Waveform Components. *Chinese Journal of Geophysics (in Chinese)* **2013**, 56, 2771-2782, doi:10.6038/cjg20130825.

26. Luo, Y.H.; Xia, J.H.; Miller, R.D.; Xu, Y.X.; Liu, J.P.; Liu, Q.S. Rayleigh-Wave Mode Separation by High-Resolution Linear Radon Transform. *Geophysical Journal International* **2009**, 179, 254–264, doi:10.1111/j.1365-246x.2009.04277.x

27. Jiang, X.X.; Zheng, F.; Jia, H.Q.; Lin, J.; Yang, H.Y. Time-Domain Hyperbolic Radon Transform for Separation of P-P and P-Sv Wavefields. *Studia Geophysica Et Geodaetica* **2016**, 60, 91-111, doi:10.1007/s11200-015-0735-y.

28. Scales, J.A.; Gerztenkorn, A.; Treitel, S. Fast Ip Solution of Large, Sparse, Linear Systems: Application to Seismic Travel Time Tomography. *Journal of Computational Physics* **1988**, 75, 314-333, doi:10.1016/0021-9991(88)90115-5.

29. Turner, G. Aliasing in the Tau-P Transform and the Removal of Spatially Aliased Coherent Noise. *Geophysics* **1990**, 55, 1496-1503, doi:10.1190/1.1442797

30. Ibrahim, A.; Sacchi, M.D. Simultaneous Source Separation Using a Robust Radon Transform. *Geophysics* **2014**, 79, V1-V11, doi:10.1190/geo2013-0168.1.

31. Trad, D.; Ulrych, T.J.; Sacchi, M.D. Accurate Interpolation with High-Resolution Time-Variant Radon Transforms. *Geophysics* **2002**, 67, 25-26, doi:10.1190/1.1468626.

32. Sabbione, J.I.; Sacchi, M.D. Restricted Model Domain Time Radon Transforms. *Geophysics* **2016**, 81, A17-A21, doi:10.1190/geo2016-0270.1.

33. Sabbione, J.I.; Velis, D.R.; Sacchi, M.D. Microseismic Data Denoising via an Apex-Shifted Hyperbolic Radon Transform. In Proceeding of SEG Technical Program Expanded Abstracts, Houston, USA, 2013; pp. 2155-2161, doi:10.1190/segam2013-1414.1.

34. Chen, X.; Sun, J.Z. An Improved Equivalent Homogenous Half-Space Method and Reverse Fitting Analysis of Rayleigh Wave Dispersion Curves. *Chinese Journal of Geophysics (in Chinese)* **2006**, 49, 489–498, doi:10.3321/j.issn:0001-5733.2006.02.033.